

Correlative Analysis of Ion-Concentration Profile and Surface Nanoscale Topography Changes Using Operando Scanning Ion Conductance Microscopy

Yasufumi Takahashi,* Daiko Takamatsu, Yuri Korchev, and Takeshi Fukuma



Cite This: *JACS Au* 2023, 3, 1089–1099



Read Online

ACCESS |

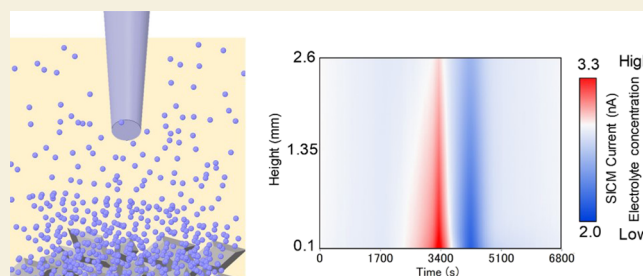
Metrics & More

Article Recommendations

Supporting Information

ABSTRACT: Although various spectroscopic methods have been developed to capture ion-concentration profile changes, it is still difficult to visualize the ion-concentration profile and surface topographical changes simultaneously during the charging/discharging of lithium-ion batteries (LIBs). To tackle this issue, we have developed an *operando* scanning ion conductance microscopy (SICM) method that can directly visualize an ion-concentration profile and surface topography using a SICM nanopipette while controlling the sample potential or current with a potentiostat for characterizing the polarization state during charging/discharging. Using *operando* SICM on the negative electrode (anode) of LIBs, we have characterized ion-concentration profile changes and the reversible volume changes related to the phase transition during cyclic voltammetry (CV) and charge/discharge of the graphite anode. *Operando* SICM is a versatile technique that is likely to be of major value for evaluating the correlation between the electrolyte concentration profile and nanoscale surface topography changes.

KEYWORDS: SICM, *operando* imaging, electrochemical imaging, nanopipette, graphite anode, lithium-ion battery



INTRODUCTION

The electrochemical reactions and topography changes of lithium-ion batteries (LIBs) involve non-equilibrium and multi-step phenomena such as Li^+ ion transport, Li^+ solvation/desolvation, Li^+ intercalation, structural changes of cathode/anode, formation and deposition of by-products, and expansion of cathode/anode. Capturing such multi-step and time-dependent changes with a relevant spatiotemporal resolution enables optimizing the operating conditions and the cathode/separator/anode structure, and identifying the additives for proper solid–electrolyte interphase (SEI) formation taking into account non-equilibrium changes.

Currently, several methods have been used to monitor the ion-concentration profile, including *in situ* nuclear magnetic resonance (NMR),^{1–4} magnetic resonance imaging (MRI),^{5–7} neutron scattering,⁸ X-ray imaging,^{9–11} and Raman microscopy.^{12–14} *In situ* surface-sensitive X-ray absorption spectroscopy has clarified that Co reduction at the LiCoO_2 surface resulting from electrolyte contact causes initial degradation.^{15,16} Scanning transmission X-ray microscopy has been developed to probe the spatiotemporal evolution of Li composition and intercalation rate within primary particles.¹⁷ Electron beam irradiation and electron energy-loss spectroscopy have been used to sense the Li-intercalation reactions in the local region.¹⁸ The volume change of the LIB anode has been estimated by X-Ray diffraction,¹⁹ neutron diffraction,²⁰ and neutron transmission Bragg-edge imaging.²¹ However, it is

difficult for most analytical tools to perform the correlative analysis of topographical changes and ion-concentration profile during charging/discharging because of the difference in the measurement conditions and scale limitations of each analytical tool.

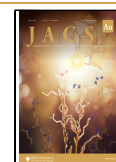
Scanning probe microscopy (SPM) is an effective tool for nanoscale correlative analysis as it allows the simultaneous imaging of sample surface properties and morphology. Conductive atomic force microscopy (c-AFM) can visualize conductance changes and topographical changes simultaneously.²² The double-layer structure of two ionic liquids has also been directly probed using AFM.²³ Electrochemical strain microscopy can visualize surface topography and Li diffusion.^{24–26} *Operando* AFM can characterize the mechanical response of the sample during electrochemical cycling and its correlation with the device's electrochemical performance.^{27–29} Scanning electrochemical microscopy (SECM) can visualize the SEI formation.^{30–35} Scanning electrochemical cell microscopy (SECCM), which uses a nanopipette capable

Received: December 9, 2022

Revised: February 16, 2023

Accepted: February 17, 2023

Published: February 27, 2023



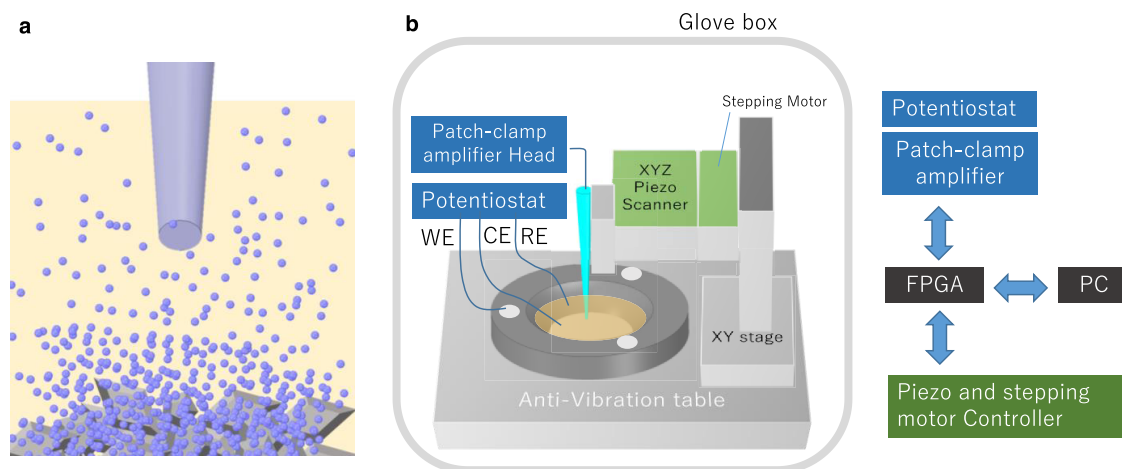


Figure 1. Scheme of the *operando* SICM. (a) Scheme of an ion-concentration measurement using the nanopipette. (b) System diagram of *operando* SICM. The potential of the sample and SICM Li metal wire electrode were controlled by the potentiostat and patch-clamp current amplifier, respectively. To perform the *operando* measurement, the potential of the potentiostat and current amplifier was synchronized to keep the potential of the current amplifier constant during the electrochemical measurement. The whole system was placed in a glovebox to keep the low oxygen and dew point temperature.

of acting as a mobile sub-micro electrochemical cell, can visualize the surface reactivity of the cathode and anode material at a sub-micrometer resolution.^{36–41} SECCM can be easily performed for high-resolution electrochemical imaging because a meniscus-shaped electrochemical cell forms on the sample surface via a nanopipette. However, SECCM cannot visualize the vertical chemical distribution and structural changes (such as the formation of dendrites) because the whole sample does not immerse in the solution. Such ion-concentration profile changes derived from the whole LIB reaction are still a critical issue for imaging by SPMs.

Scanning ion conductance microscopy (SICM), which uses a nanopipette as a probe, is a promising technology to visualize the ion-concentration profile on the sub-micro-scale. SICM is known as a noncontact topographic imaging technique in solution because ion current is used as feedback for probe–sample distance control.^{42–45} For convoluted sample imaging, hopping mode, and similar techniques have been developed to avoid nanopipette–sample contact.^{44,46} The hopping mode involves approaching and withdrawing the nanopipette at all measurement points. Hersam and co-workers have used SICM for LIB analysis.⁴⁷ The local ion current measurement using a nanopipette was effective not only for topographic imaging but also for monitoring local ion permeability,⁴⁸ three-dimensional (3D) ion distribution,^{49,50} ionic reactions,⁵¹ and surface charge.^{52–54} Local ion delivery is also an attractive application of SICM.^{55–57} However, SICM has been used principally for live cell measurements. Simultaneous potential and current control of SICM and LIB materials have been difficult for conventional SICM.

Nanopipette-based electrochemical measurement is effective for characterizing the local ion concentration. The first nanopipette-based electrochemical measurement was reported by Bard and co-workers.⁵⁸ They observed the nonlinear potential–current response, which is called the rectification effect, when they used a tiny quartz nanopipette for cyclic voltammetry (CV) measurement. The relationship between the electrolyte concentration gradient and rectification was also reported.^{59,60} Siwy and co-workers investigated Li^+ transfer in aprotic solvents using LiClO_4 as an electrolyte.⁶¹ However, there is no report that evaluates the electrolyte concentration

gradient during charge/discharge of the anode/cathode of LIBs by SICM.

In this work, we have developed an *operando* SICM system for directly visualizing the ion-concentration profile and nanoscale topographic changes at an anode surface during the CV and charge/discharge characteristics. We have characterized the composite electrode of the graphite anode by using *operando* SICM. To perform the *operando* measurement by SICM, we have developed hardware and software that can independently control the potential of the LIB electrode and SICM working electrode using a potentiostat and the current amplifier, respectively. We have also constructed a characterization technique for a three-dimensional ion-concentration profile.

EXPERIMENTAL SECTION

Operando SICM Setup

The piezo scanner of the SICM setup has been reported in our previous work.⁴⁵ The glass nanopipettes (aperture inner radius, 50 nm) were fabricated from borosilicate glass capillaries (GC100F-15, Harvard Apparatus) using a CO_2 laser puller (Model P-2000, Sutter Instruments). The SICM uses a nanopipette probe containing 1 M LiClO_4 in a 1:2 volumetric mixture of ethylene carbonate (EC) and diethylene carbonate (DEC). Li metal-coated Cu wire was inserted into the nanopipette and used as the SICM working electrode. For the *operando* SICM measurement, sample potential, or current control during SICM current detection is essential. The potential and current of the sample LIB material (composite graphite electrode) were controlled by a potentiostat (TM-3000, EC Frontier) and a homemade Labview program. Li metal was used as reference and counter electrodes. The surface area of the sample was 0.50 cm^2 . The potentials of SICM working and LIB material working electrodes were controlled individually. The reference electrode was shared by the potentiostat and the current amplifier. The potential between the potentiostat working electrode and the current amplifier working electrode was controlled using the external bias input function of the current amplifier and Labview program. The detail of the electric circuit is described in the Supporting Information (Figure S1).

Sample Preparation

The graphite anodes were composed of a mixture of 97 wt % graphite active material, 1 wt % carboxymethyl cellulose (CMC), and 2 wt % styrene–butadiene rubber (SBR) binder. The slurry was coated onto

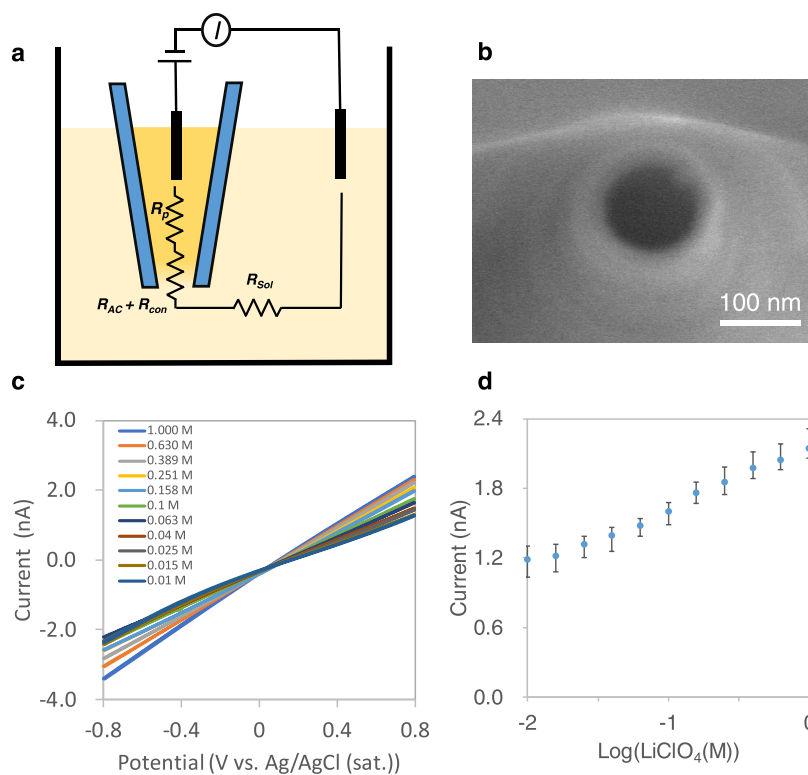


Figure 2. Characterization of the relationship between the ion current and the LiClO_4 concentration. (a) Scheme of an ion-concentration measurement using a nanopipette. The total resistance is defined as $R = R_p + R_{AC} + R_{con} + R_{sol}$. R_p is the nanopipette shunt resistance, R_{AC} is the nanopipette–sample distance-dependent resistance, R_{con} is the nanopipette around the electrolyte concentration-dependent resistance, R_{sol} is the solution resistance between the nanopipette and the reference. $R_{sol} \ll R_p + R_{AC} + R_{con}$. (b) Scanning electron microscopy image of the nanopipette, (c) Typical CVs of the nanopipette with 1.0 M LiClO_4 in EC/DEC = 1:2 (v/v) inside the nanopipette and varied LiClO_4 concentrations outside. (d) The calibration plot of LiClO_4 concentration and ion current signal at 0.7 V ($n = 3$). The measurement was performed outside of the glovebox and Ag/AgCl wire and Ag/AgCl(sat.) were used as working and reference electrodes, respectively.

a copper current collector (thickness: 10 μm), which was used as the negative electrode. The coating amount of the negative electrode layer, density, and thickness were 10.2 mg/cm, 1.56 g/cm, and 28 μm , respectively (Figure S5).

RESULTS AND DISCUSSION

To monitor the ion-concentration change on the sample surface during CV or charge/discharge, we used a half-cell system for controlling the potential or current of the composite graphite electrode with a potentiostat and a SICM nanopipette brought close to the sample surface using ion current distance control (Figure 1). During the CV of the sample, the nanopipette position was kept at 10 μm distance from the sample surface and +0.7 V was applied (vs Li/Li^+ ; all voltages in this paper quoted as vs Li/Li^+). The nanopipette–sample distance was estimated by fitting the theoretical approach curve of the previous report.⁶² The methodological improvement produced by this work is a current detection system. If both the nanopipette and sample current are in the nA range, the IR drop effect is negligible. Therefore, most of SICM previous work has been performed using a two-current amplifier system. However, the inhomogeneous ion profile distribution related to the LIB's function like high-speed charging/discharging is formed not only at the nm scale but also μm and mm scale. In the case of the mA level current measurements like the centimeter scale lithium-ion battery materials, the IR drop effect is a critical issue. Therefore, it is necessary to use the three-electrode system and an accurate potential control potentiostat is required. However, the temporal resolution of

the potentiostat for nA level current detection (tens of Hz) is not enough to control the SICM nanopipette–sample distance.

To solve this issue, we used both the patch current amplifier (high temporal resolution and accurate current detection) and the potentiostat (three-electrode system to solve the IR drop effect) to detect the current from the nanopipette and sample, respectively. In this case, the patch-clamp amplifier and the potentiostat need to share the potentiostat reference electrode. The difficulty of sharing the reference electrode is the potential control of the patch-clamp amplifier. Because the setting of the system of ground and working and reference electrodes is different between the patch-clamp amplifier and potentiostat, the potential of our potentiostat working electrode is the same as that of the potentiostat system ground. Therefore, inverted potential, which we want to apply to the potentiostat working electrode, is applied to the potentiostat reference electrode. On the other hand, the potential of the patch-clamp reference electrode is the same potential to patch-clamp system ground. Therefore, the potential of the patch-clamp working electrode adds directly to the working electrode against the patch-clamp reference electrode. The details of the electric circuit are described in the Supporting Information (Figure S1).

First of all, to investigate the relationship between the SICM ion current response and corresponding salt concentration, the SICM ion current was characterized by CV measurements when the inside of the nanopipette was kept at 1.0 M and the ambient LiClO_4 concentration was varied. The four kinds of resistances of the nanopipette-based current were measured. R_p is the nanopipette shunt and aperture size-dependent

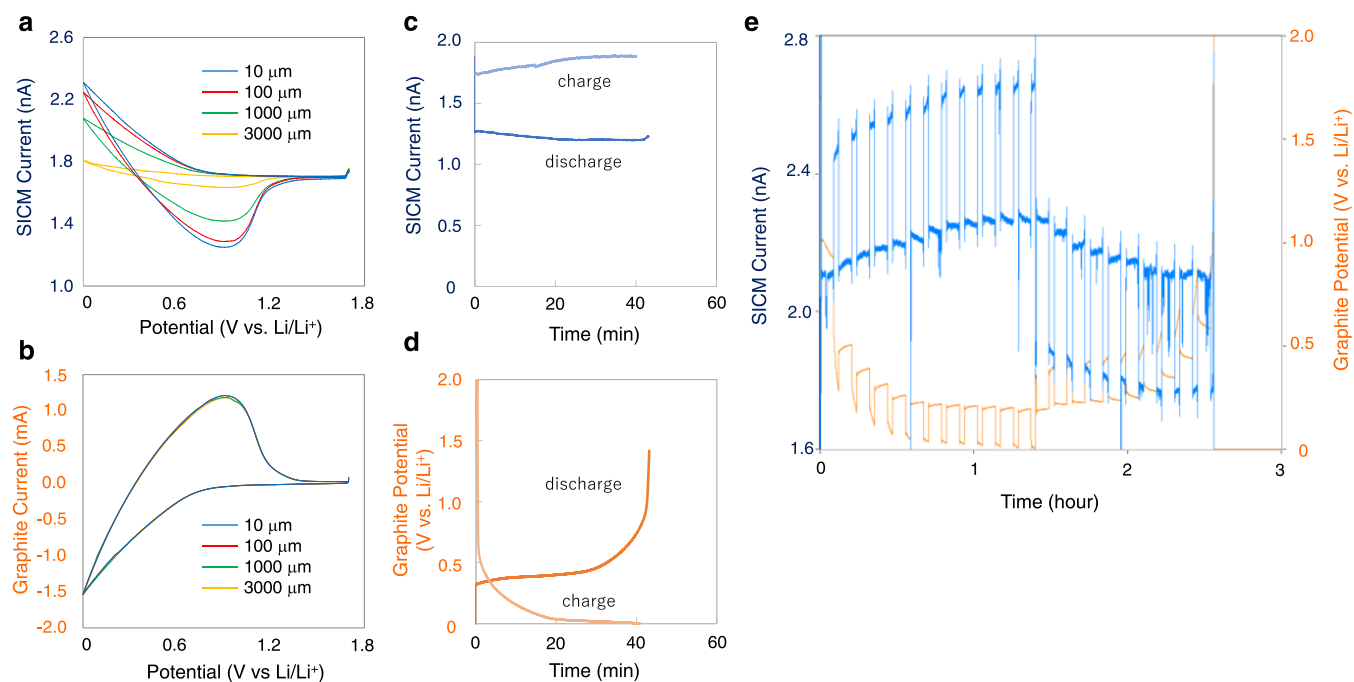


Figure 3. Ion-concentration monitoring using *operando* SICM. (a) SICM and (b) graphite anode currents during CV of the graphite anode on different nanopipette–sample distances. Scan rates were 10 mV/s. (c) SICM current and (d) graphite anode potential during the charging/discharging characteristic. The current density of the graphite anode was 0.4 mA/cm². (e) GITT of the graphite anode and SICM current measurement. The 0.8 mA/cm² pulse current was applied for 120 s. Rest time was 300 s. During the SICM ion current measurement, the potential of the nanopipette was kept at 0.7 V vs Li/Li⁺ and the nanopipette of SICM kept 10 μm away from the sample surface. The nanopipette radii were 50 nm and filled with 1.0 M LiClO₄ in EC/DEC = 1:2 (v/v).

resistance, R_{AC} is the access resistance, which depends on the nanopipette–sample distance, R_{con} is the electrolyte concentration-dependent resistance at the top of the nanopipette, and R_{sol} is the solution resistance between the nanopipette and the reference electrode (Figure 2a). The R_{sol} -related iR drop effect is ignorable for characterizing the LiClO₄ concentration and ion current relationship because the current level of the nanopipette characterization is in the nA range. Figure 2b shows the scanning electron microscopy image of the nanopipette. The size of the nanopipette aperture radius was 50 nm. In this experiment, we used a two-electrode system and performed the measurement outside of the glovebox. The Ag/AgCl wires⁶³ were inserted into the nanopipette and immersed in the bath, respectively. The nanopipette was held at an adequate distance from the substrate for measurement. Figure 2c,d shows the CV curves and ion current responses at +0.7 V of the different LiClO₄ concentrations. We observed the linear relationship between the electrolyte concentration and ion current. We also characterized the nanopipette fabrication reproducibility, stability of the ion current drift during the long-time measurement, and aperture size and I – V response relationship and confirmed the reliability of the current detection using the single nanopipette (Figures S2 and S3). These results mean that the electrolyte concentration changes can be monitored from ion current signals of the SICM nanopipette.

For characterizing the electrolyte concentration profile change by *operando* SICM, we measured the SICM current with different distances between the single nanopipette and the graphite anode during CV of the graphite anode. The potential range of CV was 0 to 1.7 V. During CV, the 50 nm radius SICM single nanopipette potential was kept at +0.7 V. The

distance between the nanopipette and the graphite anode was maintained at 10, 100, 1000, and 3000 μm, and the CV scan rate was 10 mV/s. Figure 3a,b shows the nanopipette–sample distance-dependent SICM current changes during the CV measurement of the graphite anode. The current responses of the graphite anode and the SICM were contrasting. This is due to the inhomogeneous distribution of the overall salt concentration caused by the Li⁺ migration. Ion transport in an electrolyte solution in the presence of an applied electric field is a combination of migration and diffusion. For example, during the charging of the graphite anode (i.e., Li⁺ intercalation to the graphite), the electric field causes the migration of cations (i.e., Li⁺) to the negative electrode (i.e., graphite anode). To maintain the local electroneutrality of the electrolyte solution, the anions (i.e., ClO₄[−]) concentration also to be higher near the graphite anode. At the same time, Li⁺ intercalation reaction occurs on the graphite anode surface, but the intercalation rate of Li⁺ into the graphite is slower than the ion migration, so the overall cation and anion concentration is higher on the graphite anode surface than the bulk during solution charging. Therefore, the current change of SICM became smaller when the sample–nanopipette distance increased even if the graphite anode current responses were the same. We also characterized the sample potential scan rate-dependent ion-concentration change using SICM and observed the contrasted response of the SICM current to the graphite anode's Li intercalation/(de)intercalation current (Figure S4). These results mean that the *operando* SICM is thus useful for detecting transient ion-concentration profile changes.

Ion-concentration profile detection during charge/discharge characteristics was also capable of being assessed by *operando*

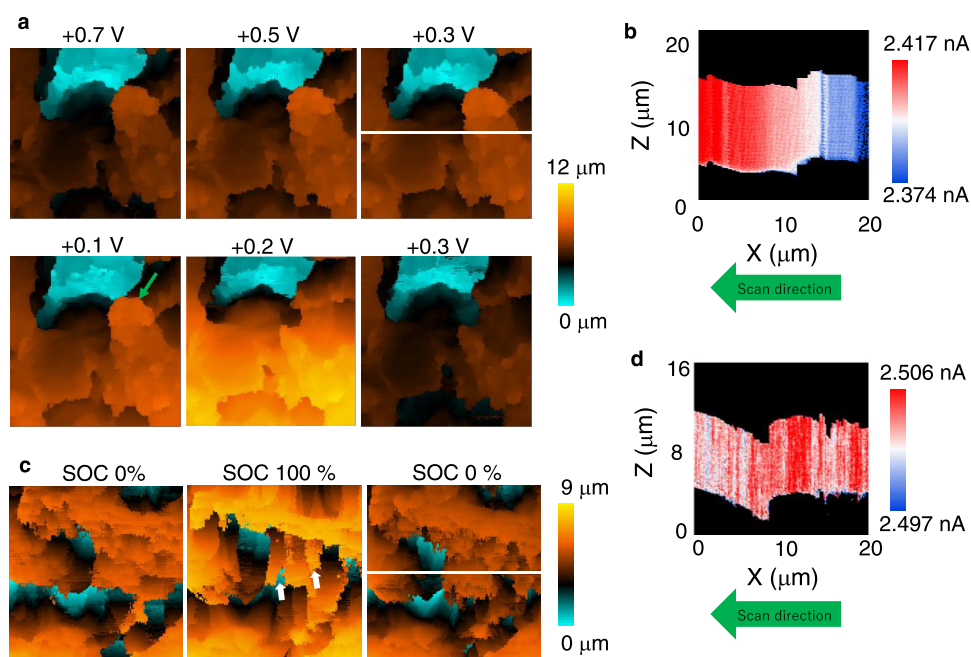


Figure 4. SICM topography and ion profile imaging of the graphite anode. (a) Time-lapse SICM topography images of the graphite anode with step potential sweep. Before imaging, the rest period was set at 5 min to suppress the double-layer capacitance current. During the SICM imaging, the graphite potential was maintained constant. The image was acquired by applying the constant voltage of 0.7 V vs Li/Li⁺. (b) XZ SICM ion current image, where the image point is shown on the white line indicated in (a). (c) SICM topography images before (SOC 0%) and after charging (SOC 100%) and discharging (SOC 0%) of the graphite anode. During SICM imaging, the graphite anode current was kept constant (0 mA). The SICM image was acquired by applying a constant voltage of 0.8 V vs Li/Li⁺ to an SICM Li electrode. (d) XZ SICM ion current image, where the image point is shown on the white line indicated in (c). Scan size and pixel numbers of a and b were 20 × 20 μm² and 128 × 128, respectively. The nanopipette radii were 50 nm and filled with 1.0 M LiClO₄ in EC/DEC = 1:2 (v/v).

SICM. In this experiment, the single nanopipette position was kept at 10 μm distance from the sample surface and had an applied potential of +0.7 V. Figure 3c,d shows the charge/discharge curve of the graphite anode while controlling the applied current at 0.4 mA/cm². Change in SICM's current corresponding to the ion-concentration change was observed in both the charging and discharging processes. Notably, unlike the case of CV, the ion current increased or decreased at an almost constant rate regardless of the change in the potential on the graphite anode. In charging/discharging at a low rate, the ion-concentration profile had to be in a steady state because of the balance of ion migration and diffusion. On the other hand, in CV with a fast scan rate, the change in the SICM current was considered to be large because the electric field is constantly changing and the ion migration and diffusion are in constant conflict and imbalance.

Operando SICM can measure the local ion-concentration profile as an ion current under the condition that the sample is forcibly controlled by a potentiostat so that a constant potential or current. In this case, the ion current response corresponds to the electrochemical potential (ion-concentration profile and electrostatic potential of the sample). It is also possible to measure only the ion concentration near the sample by allowing no current to pass through the sample. This is chemical potential measurement. To characterize the electrochemical potential and chemical potential change during charging and discharging, galvanostatic intermittent titration technique (GITT) measurements were performed. We observed the SICM ion current changes when switching the constant current (0.8 mA/cm²) to open circuit potential (OCP). The SICM current responses were corresponding to electrochemical potential and chemical potential, respectively.

The SICM current change before and after applying the pulse current to the graphite anode was 0.35 nA, which was constant regardless of the graphite with state of charge (SOC). In addition, during the OCP measurement, a change in graphite potential was observed, but no significant change was observed in the SICM current. It is thought that the concentration gradient formed during the charging/discharging can be kept constant by setting the graphite anode current as 0 mA. This result means the electrolyte concentration profile can be measured as a SICM current and electrochemical potential and chemical potential can be distinguished by GITT.

To confirm the surface topographic changes of the graphite anode during charging/discharging, the potential of the graphite anode was changed by 200 mV steps from 1.7 to 0.1 V and from 0.2 to 1.6 V imaged by SICM. During imaging, the 50 nm radius SICM single nanopipette potential was kept at +0.7 V. Before the SICM measurement, we set a 5 min rest period to suppress the double-layer capacitance current, which is induced by the potential step. Figure 4 shows the time-lapse of SICM images of the graphite anode obtained by changing the potential. The SICM topographic image of the graphite anode of the stacked polyhedral flake plates with dimensions of 3–4 μm was in good agreement with the scanning electron microscopy image (Figure S5). The hopping mode scanning algorithm and SICM noncontact distance control feature are effective in capturing the topographic image of the high-roughness graphite anode. From 1.7 to 0.9 V, we could not observe clear topographic changes. From 0.9 to 0.1 V, we found the volume expansion related to the phase transition. Notably, the structural change was observed in the image of 0.2 V. The root-mean-square roughness (R_q) values of +0.7, +0.5, +0.3, and +0.1 V topographic images were 1.27, 1.30, 1.32, and

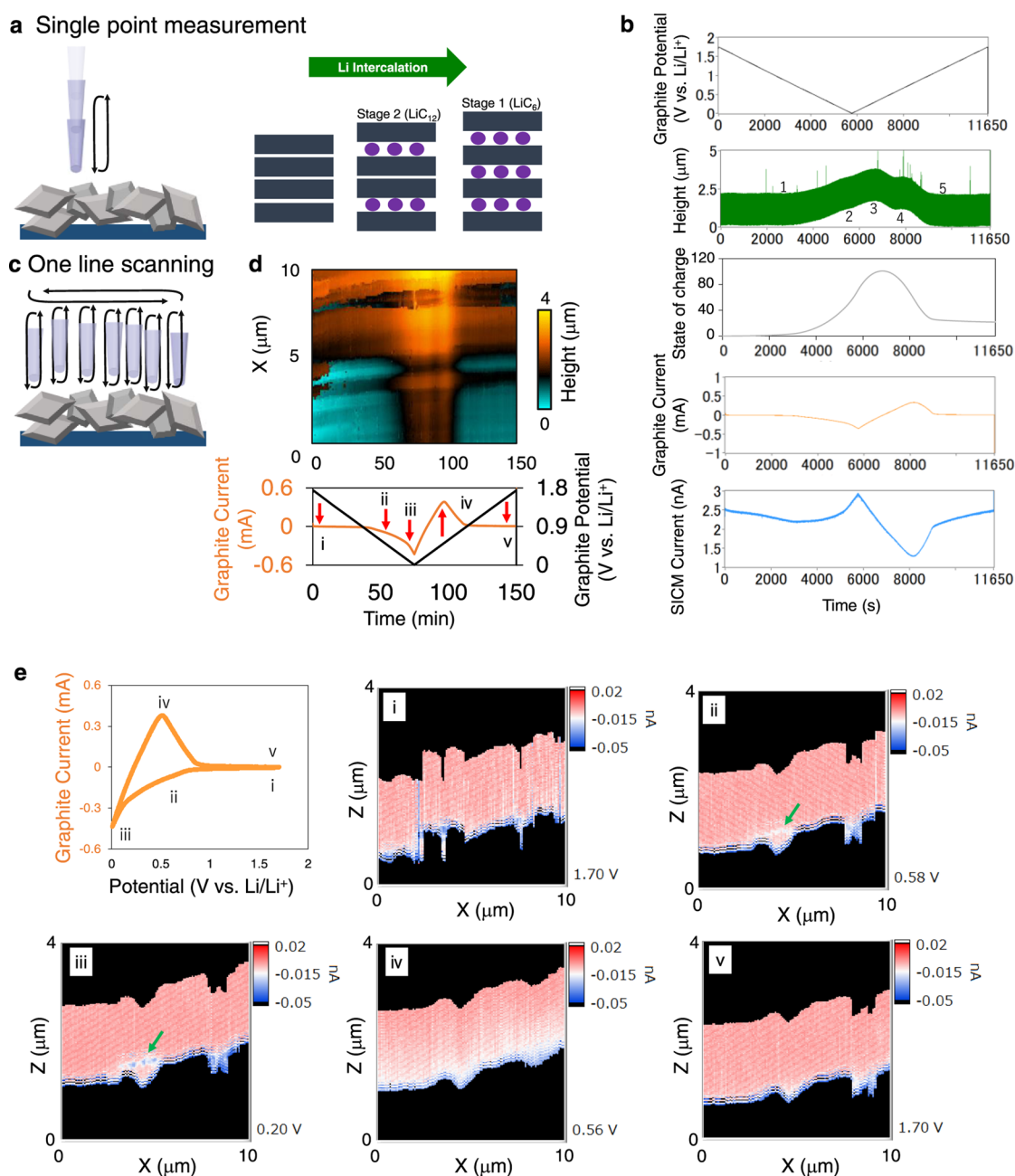


Figure 5. Volume change monitoring during the CV of the graphite anode by *operando* SICM. (a) Scheme of the single point measurement. (b) Time course of the potential, height, state of charge, carbon anode current, and SICM current during the CV. (c) Scheme of the continuous one-line scanning measurement. (d) Time course of the one-line height image, carbon anode current, and SICM current during the CV. The sweep rate was 0.3 mV/s. (e) SICM ion current XZ images, where the image points are shown in (d). Hopping amplitude and the falling rate of SICM were 2000 nm and 30 nm/ms, respectively. The nanopipette radii were 50 nm and filled with 1.0 M LiClO₄ in EC/DEC = 1:2 (v/v). Height monitoring was achieved by applying a constant voltage of 0.7 V vs Li/Li⁺.

1.31 μm , respectively. The green arrow shows the detachment region of the graphite polyhedral flake plate. We also observed shrinkage of the structure from 0.2 to 1.6 V. R_q values of the +0.2 and +0.3 V topographic images were 1.32 and 1.09 μm , respectively. We then reconstructed the SICM ion current signal during the imaging and characterized the microscale ion current profile as images (Figure 4b). SICM current is affected by the current flow of the graphite anode. Thus, it is difficult to visualize electrolyte distribution. To capture the ion-concentration profile, the sample needs to be controlled as OCP.

To characterize the surface topographic changes and ion-concentration profile after charging and discharging of the

graphite anode, we controlled the sample potential as OCP and imaged the graphite's topography. During imaging, the 50 nm radius SICM single nanopipette potential was kept at +0.8 V. Figure 4c shows the result. First, the graphite anode was discharged to 1.7 V of the current density with 0.4 mA/cm² (i.e., state of charge (SOC) was 0%). Undulating graphite topography was visualized by the hopping mode SICM. The R_q value was 1.40 μm . Then, the graphite anode was charged to 0 V of the current density with 0.4 mA/cm² (i.e., SOC was 100%) and kept at the OCP to image the topography by SICM. The white arrow shows the huge structurally changed regions. These changes looked like vertical expansion

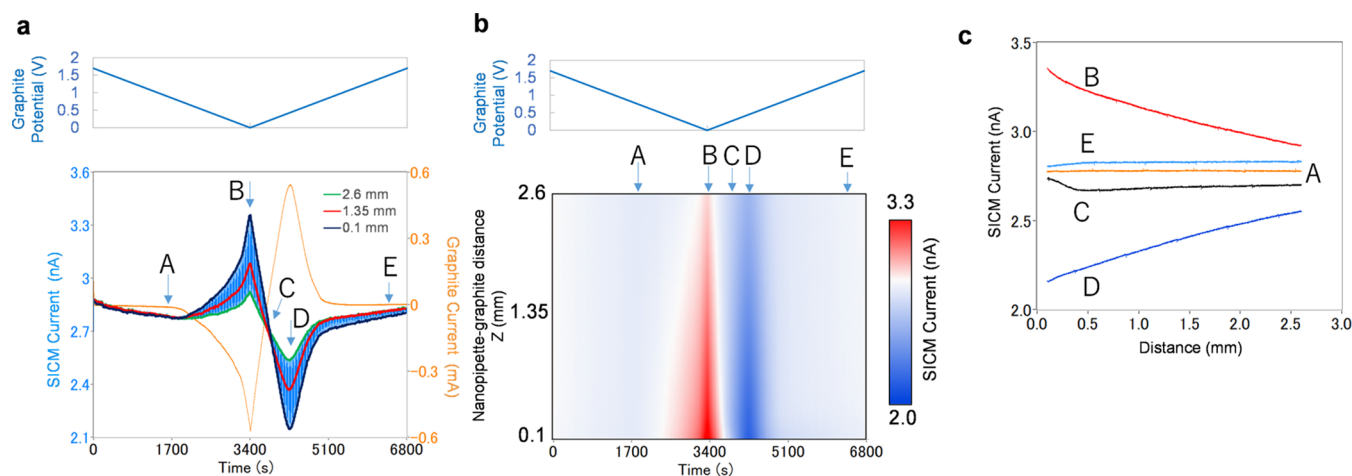


Figure 6. Millimeter-scale ion-concentration profile monitoring during the CV of the graphite anode by *operando* SICM. (a) Time course signals and SICM currents during the CV. The SICM current responses with the nanopipette–sample distances of 0.1, 1.35, and 2.6 mm were picked up and showed as a blue, red, and green line, respectively. (b) Time-course image of the SICM height and ion current during the CV. (c) Approach curves at points A–E of (a, b). The sweep rate was 0.5 mV/s. Hopping amplitude and the falling/withdrawing rate of the nanopipette were 2.5 mm and 0.5 mm/s, respectively. The nanopipette radii were 50 nm and filled with 1.0 M LiClO₄ in EC/DEC = 1:2 (v/v). The SICM ion current was acquired by applying a constant voltage of 0.7 V vs Li/Li⁺.

of the columnar structures. The R_q value was also increased to 1.55 μm . To control the sample potential as an OCP was effective to visualize the topographic changes before and after charging. Finally, we discharged the graphite anode again (SOC was 0%). Some structural changes returned to their original state because of the phase transition, but a part of the structure did not. Such irreversible volume changes might cause degradation. The R_q value was 1.12 μm . We then characterized the SICM ion current signal during imaging as XZ images (Figure 4d). The XZ SICM current image was almost uniform. This result means that the electrolyte diffusion is fast enough in the micrometer-scale region of the electrode surface, and observing the concentration profile requires millimeter-scale measurement.

To evaluate the spatial resolution of SICM, we characterized HOPG by SICM. In this experiment, commercial HOPG (NT-MDT GRBS/0.6) was used for SICM imaging. During the imaging, the 50 nm radius SICM single nanopipette potential was kept at +0.8 V. To find the step edge, we measured the topographic image after several times charging/discharging cycled HOPG (Figure S6a). The step edge was clearly visualized. We averaged the height in the red square region to estimate the step edge height (Figure S6b). The step edge height was 10 nm. The step edge swellings were reported as being formed by decomposition products of co-intercalated solvent molecules between graphite layers beneath the surface. This is in agreement with the previous report.^{64–66} These results mean that the SICM spatial resolution is beyond that of optical microscopy.

The volume change is one of the main factors for deterioration of LIBs. Therefore, it is important to understand at what potential the volume change of graphite occurs and how the ion-concentration profile changes at that time during the operation, to prevent deterioration and perform efficient charging and discharging. The volume change during charging and discharging of graphite electrodes is known to be due to the formation of SEI and the phase transition of graphite. The formation reaction of SEI is an irreversible reaction and occurs from a potential of around 0.75 V.²⁹ On one hand, the phase

transition is reversible, producing a stepwise volume change at potentials below 0.2 V.^{19,67}

To estimate the volume change of the graphite anode during CV in real-time, we were not able to set the rest period. Therefore, we monitored the sample height continuously at the single point on the graphite anode by hopping the SICM's single nanopipette. To eliminate the vertical direction artifact of the SICM measurement that depends on changes in the electrolyte concentration, the setpoint was 98% (2.0% decrease from the reference current), a significantly large value for the SICM distance control. Hopping amplitude and falling rates were 2000 nm and 30 nm/ms, respectively. CV sweep rate of the graphite anode was 0.3 mV/s and CV was cycled twice before the *operando* SICM experiment. In this experiment, a 50 nm radius single nanopipette was used. Figure 5a shows a schematic of the single-point height change monitoring during the CV of the graphite anode by SICM. Figure 5b shows the time course of the potential, height, graphite anode current, and SICM current during the CV. To characterize the effect of ion current change during the CV for nanopipette–sample control, we analyzed the maximum ion current change during ten continuous hopping processes. The ion-current change of the process was 0.5%. This value is relatively small in relation to the setpoint. Therefore, under these experimental conditions, we could avoid an artifact in height measurement due to changes in the ion concentration.

During CV, the graphite anode volume change was observed from +0.8 V (Figure 5b, Point 1). This volume change resulted from SEI formation. This volume expansion was continued until 50% SOC (Figure 5b, Point 2), however, the slope of the volume expansion was increased by around +0.2 V. This slope change corresponded with the phase transition from stage 1L-4L-3L-2L to stage 2.¹⁹ The volume then expanded again until the SOC reached 100%. This volume change corresponded to the phase transition from stage 2 to stage 1 (Figure 5b Point 4). The volume shrinkage corresponding with the phase transition from stage 1 to stage 2 was observed until 50% SOC. In the same manner, stage 2 to 1L-4L-3L-2L stage was also observed (Figure 5b Point 5). The volume expansion was

estimated from the height change and thickness of the graphite anode (28 μm). The volume changes of stage 1L-4L-3L-2L to stage 2 and stage 2 to stage 1 were 4.11% (1.15 μm) and 1.78% (0.50 μm), respectively. The total volume change was 5.89%. Since it is a graphite compound electrode, grains of graphite point in different directions. Therefore, the rate of volume change itself is not important. However, the potential at which this volume change occurs was the same even when we performed similar measurements ($n = 3$).

We also performed time-lapse one-line scanning for visualizing the volume change during the charge/discharge (Figure 5d). CV sweep rate of the graphite anode was 0.3 mV/s and CV was cycled twice before the *operando* SICM experiment. The vertical axis shows the X position of the one-line scan, the horizontal axis shows the time course, and the color contrast shows the sample height. The reversible volume change-related phase transition was clearly visualized by SICM. We performed the same experiment three times and observed similar volume changes. We then reconstructed the SICM ion current signal during the time-lapse imaging and characterized the microscale ion current profile as images. In most cases, the transient ion current change caused by the potential change of the graphite anode was dominant. To remove this transient ion current change effect, we normalized the ion current signal of XZ images by evaluating ion current difference from the mode value at each of the approaching curves. This processing is effective at removing the transient ion current changes and easy to visualize the ion current gradient. We observed a low ion current region around the depressed structure during the CV (Figure 5e, green arrows and Supporting Movies 1). We also found the 250–300 nm region near the electrode where the ion current decreases. These results suggest that *operando* SICM is an effective tool for characterizing such micrometer-scale height and electrolyte profile changes during charging/discharging.

A millimeter-scale ion-concentration profile can also be monitored by *operando* SICM. The nanopipette position was controlled by a stepping motor and the measurement range and velocity were 2.5 mm and 0.5 mm/s, respectively. In this experiment, a 50 nm radius single nanopipette was used. The nanopipette–graphite distance was controlled from 0.1 mm to 2.6 mm. The CV sweep rate was 0.5 mV/s and CV was cycled twice before the *operando* SICM experiment. Figure 6a shows the time course of the signals of the graphite anode and SICM current during the CV. Figure 6b shows the time-course image of the nanopipette–sample distance and SICM ion current during the CV. Figure 6c shows the characteristic approach at points A–E of Figure 6a. The time-course image of the SICM current is easy to understand as the counter ion profile changed during CV in the millimeter scale. During the forward scan, the SICM's current change was not observed until 0.8 V (Figure 6c Point A). The SICM current was then increased when the nanopipette was close to the sample because of the increase in the overall salt concentration at the graphite surface (Figure 6c, Point B). This trend was changed at +0.5 V of the reverse scan (Figure 6c, point C). The polarized counter ion distribution was observed only within 0.4 mm from the sample surface. This is because counter ion concentration decreased due to the applied potential to the graphite anode. The SICM current response decreased when the nanopipette was close to the sample because the counter ion moved to the counter electrode surface (Figure 6c, Point D). At the end of the CV, the counter ion-concentration profile was almost uniform

(Figure 6c, Point E). From these results, we conclude that *operando* SICM is also useful in monitoring the millimeter-scale ion profile change with sample charging/discharging current responses during the CV of the sample.

CONCLUSIONS

In this study, we have established *operando* SICM for correlative analysis of the ion-concentration change and nanoscale topography change of LIBs' electrolyte solution during charging and discharging. We first characterized the relationship between Li^+ concentration and SICM ion current. We then visualized the topographic changes and characterized the local ion current changes during charge/discharge and CV using *operando* SICM. Notably, we observed reversible phase transition-related volume change during the CV measurement of the graphite electrode. Reversible and irreversible topographic changes and millimeter-scale ion-concentration profiles were also visualized clearly by SICM. The spatial resolution of SICM is beyond the optical limit and this enabled us to visualize the step edges of HOPG. *Operando* SICM has the potential to unveil the LIBs' non-equilibrium mechanism and bottleneck processes such as dendrite formation by correlative analysis of the dendrite formation and ion concentration for optimizing the separator structure.

ASSOCIATED CONTENT

Supporting Information

The Supporting Information is available free of charge at <https://pubs.acs.org/doi/10.1021/jacsau.2c00677>.

Electrochemical movie of the XZ ion concentration profile changes during the CV (MP4)

Circuit of the electrochemical measurement system of *operando* SICM; reliability and stability test of the ion current detection of the nanopipettes; characterization of the variety of the nanopipette size and IV responses; sweep-rate dependency; SEM images of the graphite anode; and SICM topography images of HOPG (PDF)

AUTHOR INFORMATION

Corresponding Author

Yasufumi Takahashi – Department of Electronics, Graduate School of Engineering, Nagoya University, Nagoya 464-8603, Japan; WPI Nano Life Science Institute (WPI-NanoLSI), Kanazawa University, Kanazawa 920-1192, Japan; orcid.org/0000-0003-2834-8300; Email: takahashi.yasufumi.v5@f.mail.nagoya-u.ac.jp

Authors

Daiko Takamatsu – Center for Exploratory Research, Research & Development Group, Hitachi, Ltd., Saitama 350-0395, Japan

Yuri Korchev – WPI Nano Life Science Institute (WPI-NanoLSI), Kanazawa University, Kanazawa 920-1192, Japan; Department of Medicine, Imperial College London, London W12 0NN, United Kingdom

Takeshi Fukuma – WPI Nano Life Science Institute (WPI-NanoLSI), Kanazawa University, Kanazawa 920-1192, Japan; Division of Electrical Engineering and Computer Science, Kanazawa University, Kanazawa 920-1192, Japan; orcid.org/0000-0001-8971-6002

Complete contact information is available at:

<https://pubs.acs.org/10.1021/jacsau.2c00677>

Author Contributions

Y.T., and D.T. designed research; Y.T. performed research; Y.T. analyzed data; and Y.T., D.T., Y.K., and T.F. wrote the paper.

Notes

The authors declare no competing financial interest.

ACKNOWLEDGMENTS

A Grant-in-Aid for Scientific Research (A) (19H00915), a Grant-in-Aid for Young Scientists (A) (15H05422), a Grant-in-Aid for Exploratory Research (15K13263 and 20K21141), and a Grant-in-Aid for Scientific Research on Innovative Areas (16H00885) from the Japan Society for the Promotion of Science (JSPS), a World Premier International Research Center Initiative (WPI), MEXT, Japan, and Asahi Glass Foundation, a Grant-in-Aid for Young Scientists provided by Hokuriku bank, Murata Science Foundation, and Toyota Mobility Foundation (TMF) are all thankfully acknowledged for financial support.

REFERENCES

- (1) Klett, M.; Giesecke, M.; Nyman, A.; Hallberg, F.; Lindström, R. W.; Lindbergh, G.; Furó, I. Quantifying Mass Transport during Polarization in a Li Ion Battery Electrolyte by in Situ ^7Li NMR Imaging. *J. Am. Chem. Soc.* **2012**, *134*, 14654–14657.
- (2) Krachkovskiy, S. A.; Pauric, A. D.; Halalay, I. C.; Goward, G. R. Slice-Selective NMR Diffusion Measurements: A Robust and Reliable Tool for In Situ Characterization of Ion-Transport Properties in Lithium-Ion Battery Electrolytes. *J. Phys. Chem. Lett.* **2013**, *4*, 3940–3944.
- (3) Hayamizu, K.; Seki, S.; Miyashiro, H.; Kobayashi, Y. Direct in Situ Observation of Dynamic Transport for Electrolyte Components by NMR Combined with Electrochemical Measurements. *J. Phys. Chem. B* **2006**, *110*, 22302–22305.
- (4) Krachkovskiy, S. A.; Foster, J. M.; Bazak, J. D.; Balcom, B. J.; Goward, G. R. Operando Mapping of Li Concentration Profiles and Phase Transformations in Graphite Electrodes by Magnetic Resonance Imaging and Nuclear Magnetic Resonance Spectroscopy. *J. Phys. Chem. C* **2018**, *122*, 21784–21791.
- (5) Chang, H. J.; Ilott, A. J.; Trease, N. M.; Mohammadi, M.; Jerschow, A.; Grey, C. P. Correlating Microstructural Lithium Metal Growth with Electrolyte Salt Depletion in Lithium Batteries Using ^7Li MRI. *J. Am. Chem. Soc.* **2015**, *137*, 15209–15216.
- (6) Krachkovskiy, S. A.; Bazak, J. D.; Werhun, P.; Balcom, B. J.; Halalay, I. C.; Goward, G. R. Visualization of Steady-State Ionic Concentration Profiles Formed in Electrolytes during Li-Ion Battery Operation and Determination of Mass-Transport Properties by in Situ Magnetic Resonance Imaging. *J. Am. Chem. Soc.* **2016**, *138*, 7992–7999.
- (7) Bazak, J. D.; Krachkovskiy, S. A.; Goward, G. R. Multi-Temperature in Situ Magnetic Resonance Imaging of Polarization and Salt Precipitation in Lithium-Ion Battery Electrolytes. *J. Phys. Chem. C* **2017**, *121*, 20704–20713.
- (8) Jafta, C. J.; Sun, X.-G.; Veith, G. M.; Jensen, G. V.; Mahurin, S. M.; Paranthaman, M. P.; Dai, S.; Bridges, C. A. Probing microstructure and electrolyte concentration dependent cell chemistry via operando small angle neutron scattering. *Energy Environ. Sci.* **2019**, *12*, 1866–1877.
- (9) Takamatsu, D.; Yoneyama, A.; Asari, Y.; Hirano, T. Quantitative Visualization of Salt Concentration Distributions in Lithium-Ion Battery Electrolytes during Battery Operation Using X-ray Phase Imaging. *J. Am. Chem. Soc.* **2018**, *140*, 1608–1611.
- (10) Dawkins, J. I. G.; Ghavidel, M. Z.; Chhin, D.; Beaulieu, I.; Hossain, M. S.; Feng, R.; Mauzeroll, J.; Schougaard, S. B. Operando Tracking of Solution-Phase Concentration Profiles in Li-Ion Battery Positive Electrodes Using X-ray Fluorescence. *Anal. Chem.* **2020**, *92*, 10908–10912.
- (11) Mühlbauer, M. J.; Petz, D.; Baran, V.; Dolotko, O.; Hofmann, M.; Kostecki, R.; Senyshyn, A. Inhomogeneous distribution of lithium and electrolyte in aged Li-ion cylindrical cells. *J. Power Sources* **2020**, *475*, No. 228690.
- (12) Forster, J. D.; Harris, S. J.; Urban, J. J. Mapping Li^+ Concentration and Transport via In Situ Confocal Raman Microscopy. *J. Phys. Chem. Lett.* **2014**, *5*, 2007–2011.
- (13) Wei, Z.; Salehi, A.; Lin, G.; Hu, J.; Jin, X.; Agar, E.; Liu, F. Probing Li-ion concentration in an operating lithium ion battery using in situ Raman spectroscopy. *J. Power Sources* **2020**, *449*, No. 227361.
- (14) Cheng, Q.; Wei, L.; Liu, Z.; Ni, N.; Sang, Z.; Zhu, B.; Xu, W.; Chen, M.; Miao, Y.; Chen, L.-Q.; Min, W.; Yang, Y. Operando and three-dimensional visualization of anion depletion and lithium growth by stimulated Raman scattering microscopy. *Nat. Commun.* **2018**, *9*, No. 2942.
- (15) Takamatsu, D.; Nakatsutsumi, T.; Mori, S.; Orikasa, Y.; Mogi, M.; Yamashige, H.; Sato, K.; Fujimoto, T.; Takanashi, Y.; Murayama, H.; Oishi, M.; Tanida, H.; Uruga, T.; Arai, H.; Uchimoto, Y.; Ogumi, Z. Nanoscale Observation of the Electronic and Local Structures of LiCoO_2 Thin Film Electrode by Depth-Resolved X-ray Absorption Spectroscopy. *J. Phys. Chem. Lett.* **2011**, *2*, 2511–2514.
- (16) Takamatsu, D.; Koyama, Y.; Orikasa, Y.; Mori, S.; Nakatsutsumi, T.; Hirano, T.; Tanida, H.; Arai, H.; Uchimoto, Y.; Ogumi, Z. First In Situ Observation of the LiCoO_2 Electrode/Electrolyte Interface by Total-Reflection X-ray Absorption Spectroscopy. *Angew. Chem., Int. Ed.* **2012**, *51*, 11597–11601.
- (17) Lim, J.; Li, Y. Y.; Alsem, D. H.; So, H.; Lee, S. C.; Bai, P.; Cogswell, D. A.; Liu, X. Z.; Jin, N.; Yu, Y. S.; Salmon, N. J.; Shapiro, D. A.; Bazant, M. Z.; Tylliszczak, T.; Chueh, W. C. Origin and hysteresis of lithium compositional spatiodynamics within battery primary particles. *Science* **2016**, *353*, 566–571.
- (18) Kitta, M.; Kohyama, M. Nanoscale controlled Li-insertion reaction induced by scanning electron-beam irradiation in a $\text{Li}_4\text{Ti}_5\text{O}_{12}$ electrode material for lithium-ion batteries. *Phys. Chem. Chem. Phys.* **2017**, *19*, 11581–11587.
- (19) Schweidler, S.; de Biasi, L.; Schiele, A.; Hartmann, P.; Brezesinski, T.; Janek, J. Volume Changes of Graphite Anodes Revisited: A Combined Operando X-ray Diffraction and In Situ Pressure Analysis Study. *J. Phys. Chem. C* **2018**, *122*, 8829–8835.
- (20) Didier, C.; Pang, W. K.; Guo, Z.; Schmid, S.; Peterson, V. K. Phase Evolution and Intermittent Disorder in Electrochemically Lithiated Graphite Determined Using in Operando Neutron Diffraction. *Chem. Mater.* **2020**, *32*, 2518–2531.
- (21) Kamiyama, T.; Narita, Y.; Sato, H.; Ohnuma, M.; Kiyonagi, Y. Structural Change of Carbon Anode in a Lithium-ion Battery Product Associated with Charging Process Observed by Neutron Transmission Bragg-edge Imaging. *Phys. Procedia* **2017**, *88*, 27–33.
- (22) Verde, M. G.; Baggetto, L.; Balke, N.; Veith, G. M.; Seo, J. K.; Wang, Z.; Meng, Y. S. Elucidating the Phase Transformation of $\text{Li}_4\text{Ti}_5\text{O}_{12}$ Lithiation at the Nanoscale. *ACS Nano* **2016**, *10*, 4312–4321.
- (23) Hayes, R.; Borisenko, N.; Tam, M. K.; Howlett, P. C.; Endres, F.; Atkin, R. Double Layer Structure of Ionic Liquids at the Au(111) Electrode Interface: An Atomic Force Microscopy Investigation. *J. Phys. Chem. C* **2011**, *115*, 6855–6863.
- (24) Balke, N.; Jesse, S.; Kim, Y.; Adamczyk, L.; Tselev, A.; Ivanov, I. N.; Dudney, N. J.; Kalinin, S. V. Real Space Mapping of Li-Ion Transport in Amorphous Si Anodes with Nanometer Resolution. *Nano Lett.* **2010**, *10*, 3420–3425.
- (25) Balke, N.; Jesse, S.; Morozovska, A. N.; Eliseev, E.; Chung, D. W.; Kim, Y.; Adamczyk, L.; García, R. E.; Dudney, N.; Kalinin, S. V. Nanoscale mapping of ion diffusion in a lithium-ion battery cathode. *Nat. Nanotechnol.* **2010**, *5*, 749–754.
- (26) Jesse, S.; Balke, N.; Eliseev, E.; Tselev, A.; Dudney, N. J.; Morozovska, A. N.; Kalinin, S. V. Direct Mapping of Ionic Transport

- in a Si Anode on the Nanoscale: Time Domain Electrochemical Strain Spectroscopy Study. *ACS Nano* **2011**, *5*, 9682–9695.
- (27) Tsai, W.-Y.; Wang, R.; Boyd, S.; Augustyn, V.; Balke, N. Probing local electrochemistry via mechanical cyclic voltammetry curves. *Nano Energy* **2021**, *81*, No. 105592.
- (28) Wang, R.; Mitchell, J. B.; Gao, Q.; Tsai, W.-Y.; Boyd, S.; Pharr, M.; Balke, N.; Augustyn, V. Operando Atomic Force Microscopy Reveals Mechanics of Structural Water Driven Battery-to-Pseudocapacitor Transition. *ACS Nano* **2018**, *12*, 6032–6039.
- (29) Jeong, S.-K.; Inaba, M.; Mogi, R.; Iriyama, Y.; Abe, T.; Ogumi, Z. Surface Film Formation on a Graphite Negative Electrode in Lithium-Ion Batteries: Atomic Force Microscopy Study on the Effects of Film-Forming Additives in Propylene Carbonate Solutions. *Langmuir* **2001**, *17*, 8281–8286.
- (30) Zampardi, G.; Ventosa, E.; La Mantia, F.; Schuhmann, W. In situ visualization of Li-ion intercalation and formation of the solid electrolyte interphase on TiO₂ based paste electrodes using scanning electrochemical microscopy. *Chem. Commun.* **2013**, *49*, 9347–9349.
- (31) Ventosa, E.; Zampardi, G.; Flox, C.; La Mantia, F.; Schuhmann, W.; Morante, J. R. Solid electrolyte interphase in semi-solid flow batteries: a wolf in sheep's clothing. *Chem. Commun.* **2015**, *51*, 14973–14976.
- (32) Zampardi, G.; La Mantia, F.; Schuhmann, W. Determination of the formation and range of stability of the SEI on glassy carbon by local electrochemistry. *RSC Adv.* **2015**, *5*, 31166–31171.
- (33) Hui, J. S.; Burgess, M.; Zhang, J. R.; Rodriguez-Lopez, J. Layer Number Dependence of Li⁺ Intercalation on Few-Layer Graphene and Electrochemical Imaging of Its Solid-Electrolyte Interphase Evolution. *ACS Nano* **2016**, *10*, 4248–4257.
- (34) Sarbapalli, D.; Lin, Y. H.; Stafford, S.; Son, J.; Mishra, A.; Hui, J. S.; Nijamudheen, A.; Romo, A. I. B.; Gossage, Z. T.; van der Zande, A. M.; Mendoza-Cortes, J. L.; Rodriguez-Lopez, J. A Surface Modification Strategy Towards Reversible Na-ion Intercalation on Graphitic Carbon Using Fluorinated Few-Layer Graphene. *J. Electrochem. Soc.* **2022**, *169*, No. 106522.
- (35) Gossage, Z. T.; Hui, J.; Zeng, Y.; Flores-Zuleta, H.; Rodríguez-López, J. Probing the reversibility and kinetics of Li⁺ during SEI formation and (de)intercalation on edge plane graphite using ion-sensitive scanning electrochemical microscopy. *Chem. Sci.* **2019**, *10*, 10749–10754.
- (36) Takahashi, Y.; Kumatani, A.; Munakata, H.; Inomata, H.; Ito, K.; Ino, K.; Shiku, H.; Unwin, P. R.; Korchev, Y. E.; Kanamura, K.; Matsue, T. Nanoscale visualization of redox activity at lithium-ion battery cathodes. *Nat. Commun.* **2014**, *5*, No. 5450.
- (37) Inomata, H.; Takahashi, Y.; Takamatsu, D.; Kumatani, A.; Ida, H.; Shiku, H.; Matsue, T. Visualization of inhomogeneous current distribution on ZrO₂-coated LiCoO₂ thin-film electrodes using scanning electrochemical cell microscopy. *Chem. Commun.* **2019**, *55*, 545–548.
- (38) Tao, B.; Yule, L. C.; Daviddi, E.; Bentley, C. L.; Unwin, P. R. Correlative Electrochemical Microscopy of Li-Ion (De)intercalation at a Series of Individual LiMn₂O₄ Particles. *Angew. Chem., Int. Ed.* **2019**, *58*, 4606–4611.
- (39) Snowden, M. E.; Dayeh, M.; Payne, N. A.; Gervais, S.; Mauzeroll, J.; Schougaard, S. B. Measurement on isolated lithium iron phosphate particles reveals heterogeneity in material properties distribution. *J. Power Sources* **2016**, *325*, 682–689.
- (40) Dayeh, M.; Ghavidel, M. R. Z.; Mauzeroll, J.; Schougaard, S. B. Micropipette Contact Method to Investigate High-Energy Cathode Materials by using an Ionic Liquid. *ChemElectroChem* **2019**, *6*, 195–201.
- (41) Takahashi, Y.; Yamashita, T.; Takamatsu, D.; Kumatani, A.; Fukuma, T. Nanoscale kinetic imaging of lithium ion secondary battery materials using scanning electrochemical cell microscopy. *Chem. Commun.* **2020**, *56*, 9324–9327.
- (42) Zhu, C.; Huang, K.; Siepser, N. P.; Baker, L. A. Scanning Ion Conductance Microscopy. *Chem. Rev.* **2021**, *121*, 11726–11768.
- (43) Korchev, Y. E.; Bashford, C. L.; Milovanovic, M.; Vodyanoy, I.; Lab, M. J. Scanning ion conductance microscopy of living cells. *Biophys. J.* **1997**, *73*, 653–658.
- (44) Novak, P.; Li, C.; Shevchuk, A. I.; Stepanyan, R.; Caldwell, M.; Hughes, S.; Smart, T. G.; Gorelik, J.; Ostanin, V. P.; Lab, M. J.; Moss, G. W. J.; Frolenkov, G. I.; Klenerman, D.; Korchev, Y. E. Nanoscale live-cell imaging using hopping probe ion conductance microscopy. *Nat. Methods* **2009**, *6*, 279–281.
- (45) Takahashi, Y.; Zhou, Y.; Miyamoto, T.; Higashi, H.; Nakamichi, N.; Takeda, Y.; Kato, Y.; Korchev, Y.; Fukuma, T. High-Speed SICM for the Visualization of Nanoscale Dynamic Structural Changes in Hippocampal Neurons. *Anal. Chem.* **2020**, *92*, 2159–2167.
- (46) Takahashi, Y.; Murakami, Y.; Nagamine, K.; Shiku, H.; Aoyagi, S.; Yasukawa, T.; Kanzaki, M.; Matsue, T. Topographic imaging of convoluted surface of live cells by scanning ion conductance microscopy in a standing approach mode. *Phys. Chem. Chem. Phys.* **2010**, *12*, 10012–10017.
- (47) Lipson, A. L.; Ginder, R. S.; Hersam, M. C. Nanoscale In Situ Characterization of Li-ion Battery Electrochemistry Via Scanning Ion Conductance Microscopy. *Adv. Mat.* **2011**, *23*, 5613–5617.
- (48) Payne, N. A.; Dawkins, J. I. G.; Schougaard, S. B.; Mauzeroll, J. Effect of Substrate Permeability on Scanning Ion Conductance Microscopy: Uncertainty in Tip–Substrate Separation and Determination of Ionic Conductivity. *Anal. Chem.* **2019**, *91*, 15718–15725.
- (49) Takahashi, Y.; Ida, H.; Matsumae, Y.; Komaki, H.; Zhou, Y. S.; Kumatani, A.; Kanzaki, M.; Shiku, H.; Matsue, T. 3D electrochemical and ion current imaging using scanning electrochemical-scanning ion conductance microscopy. *Phys. Chem. Chem. Phys.* **2017**, *19*, 26728–26733.
- (50) Cremin, K.; Jones, B. A.; Teahan, J.; Meloni, G. N.; Perry, D.; Zeffass, C.; Asally, M.; Soyer, O. S.; Unwin, P. R. Scanning Ion Conductance Microscopy Reveals Differences in the Ionic Environments of Gram-Positive and Negative Bacteria. *Anal. Chem.* **2020**, *92*, 16024–16032.
- (51) Liu, B.; Shao, Y.; Mirkin, M. V. Dual-pipet techniques for probing ionic reactions. *Anal. Chem.* **2000**, *72*, 510–519.
- (52) McKelvey, K.; Kinnear, S. L.; Perry, D.; Momotenko, D.; Unwin, P. R. Surface Charge Mapping with a Nanopipette. *J. Am. Chem. Soc.* **2014**, *136*, 13735–13744.
- (53) Klausen, L. H.; Fuhs, T.; Dong, M. Mapping surface charge density of lipid bilayers by quantitative surface conductivity microscopy. *Nat. Commun.* **2016**, *7*, No. 12447.
- (54) Page, A.; Perry, D.; Young, P.; Mitchell, D.; Frenguelli, B. G.; Unwin, P. R. Fast Nanoscale Surface Charge Mapping with Pulsed-Potential Scanning Ion Conductance Microscopy. *Anal. Chem.* **2016**, *88*, 10854–10859.
- (55) Teahan, J.; Perry, D.; Chen, B.; McPherson, I. J.; Meloni, G. N.; Unwin, P. R. Scanning Ion Conductance Microscopy: Surface Charge Effects on Electroosmotic Flow Delivery from a Nanopipette. *Anal. Chem.* **2021**, *93*, 12281–12288.
- (56) Babakinejad, B.; Jonsson, P.; Cordoba, A. L.; Actis, P.; Novak, P.; Takahashi, Y.; Shevchuk, A.; Anand, U.; Anand, P.; Drews, A.; Ferrer-Montiel, A.; Klenerman, D.; Korchev, Y. E. Local Delivery of Molecules from a Nanopipette for Quantitative Receptor Mapping on Live Cells. *Anal. Chem.* **2013**, *85*, 9333–9342.
- (57) Piper, J. D.; Clarke, R. W.; Korchev, Y. E.; Ying, L. M.; Klenerman, D. A renewable nanosensor based on a glass nanopipette. *J. Am. Chem. Soc.* **2006**, *128*, 16462–16463.
- (58) Wei, C.; Bard, A. J.; Feldberg, S. W. Current Rectification at Quartz Nanopipet Electrodes. *Anal. Chem.* **1997**, *69*, 4627–4633.
- (59) Cheng, L.-J.; Guo, L. J. Rectified Ion Transport through Concentration Gradient in Homogeneous Silica Nanochannels. *Nano Lett.* **2007**, *7*, 3165–3171.
- (60) Deng, X. L.; Takami, T.; Son, J. W.; Kang, E. J.; Kawai, T.; Park, B. H. Effect of concentration gradient on ionic current rectification in polyethyleneimine modified glass nano-pipettes. *Sci. Rep.* **2014**, *4*, No. 4005.

(61) Plett, T.; Shi, W.; Zeng, Y.; Mann, W.; Vlassiuk, I.; Baker, L. A.; Siwy, Z. S. Rectification of nanopores in aprotic solvents – transport properties of nanopores with surface dipoles. *Nanoscale* **2015**, *7*, 19080–19091.

(62) Edwards, M. A.; Williams, C. G.; Whitworth, A. L.; Unwin, P. R. Scanning Ion Conductance Microscopy: a Model for Experimentally Realistic Conditions and Image Interpretation. *Anal. Chem.* **2009**, *81*, 4482–4492.

(63) Bentley, C. L.; Perry, D.; Unwin, P. R. Stability and Placement of Ag/AgCl Quasi-Reference Counter Electrodes in Confined Electrochemical Cells. *Anal. Chem.* **2018**, *90*, 7700–7707.

(64) Jeong, S.-K.; Inaba, M.; Abe, T.; Ogumi, Z. Surface Film Formation on Graphite Negative Electrode in Lithium-Ion Batteries: AFM Study in an Ethylene Carbonate-Based Solution. *J. Electrochem. Soc.* **2001**, *148*, No. A989.

(65) Jeong, S.-K.; Inaba, M.; Iriyama, Y.; Abe, T.; Ogumi, Z. Surface film formation on a graphite negative electrode in lithium-ion batteries: AFM study on the effects of co-solvents in ethylene carbonate-based solutions. *Electrochim. Acta* **2002**, *47*, 1975–1982.

(66) Zhang, Z.; Smith, K.; Jarvis, R.; Shearing, P. R.; Miller, T. S.; Brett, D. J. L. Operando Electrochemical Atomic Force Microscopy of Solid–Electrolyte Interphase Formation on Graphite Anodes: The Evolution of SEI Morphology and Mechanical Properties. *ACS Appl. Mater. Interfaces* **2020**, *12*, 35132–35141.

(67) Dahn, J. R. Phase diagram of Li_xC_6 . *Phys. Rev. B* **1991**, *44*, 9170–9177.